

We are IntechOpen, the world's leading publisher of Open Access books Built by scientists, for scientists

6,900

Open access books available

186,000

International authors and editors

200M

Downloads

Our authors are among the

154

Countries delivered to

TOP 1%

most cited scientists

12.2%

Contributors from top 500 universities



WEB OF SCIENCE™

Selection of our books indexed in the Book Citation Index
in Web of Science™ Core Collection (BKCI)

Interested in publishing with us?
Contact book.department@intechopen.com

Numbers displayed above are based on latest data collected.
For more information visit www.intechopen.com



Visualization of Complex Flow Structures by Matched Refractive-Index PIV Method

Kazuhisa Yuki

*Tokyo University of Science, Yamaguchi
Japan*

1. Introduction

With the development of computers and their surrounding equipments, the simulation of complicated flow structures around aircrafts will further become easier and cheaper by applying computational fluid dynamics. However, in order to judge whether the flow field obtained is reasonable or not, turbulent models and/or numerical schemes should be selected based on the comparison with experimental results. On the other hand, three-dimensional measurement of unsteady flow structures especially around obstacles with complicated geometry is still difficult due to some problems. For instance, where a three-dimensional flow structures around obstacles is visualized by a PIV technique, it is extremely difficult to grasp the whole flow-structure including the flow behind the obstacles even if transparent materials are used, because the difference of the refractive index between the working fluid and the transparent material causes distortion in the image. Therefore, in this chapter, I introduce a special visualization technique to match the refractive index of the working fluid with that of the transparent material that is called "matched refractive-index PIV measurement" and show some complicated flow fields visualized by this technique.

2. PIV visualization utilizing a matched refractive-index method

2.1 Refractive-index adjustment of NaI solution

Where the whole three-dimensional flow structure around obstacles is visualized by a PIV technique, it is necessary to match the refractive index of the working fluid with that of the obstacle material. This research employs a sodium iodide solution (NaI solution), which is easy to handle and chemically stable, as the working fluid. This solution is deliberately chosen in order to be able to adjust the refractive index of the working fluid to that of the acrylic obstacle with the index of 1.49. Normally the refractive index of this solution is not so sensitive to temperature change, so that the refractive index of the NaI solution is adjusted by changing its concentration. Figure 1 shows a light path difference caused by refraction, where a YAG laser used in the PIV measurement is irradiated to an acrylic cylinder of 30mm in diameter fixed at a center in a 10cm square acrylic box filled with the NaI solution at 30 degrees Celsius. The light path difference, δ , is measured at a location of 660mm from the back of the cylinder. The difference decreases with the increase in the NaI concentration and reaches zero at 61.6wt%. That means that the refractive index of the NaI solution completely corresponds with that of the acrylic cylinder at this concentration. In actual visualization

experiments, a refractive index at this concentration under visible light, which is 1.485, was always checked by using a portable refractometer before each experiment, because the change in the refractive index might be caused by deposition of NaI crystals onto the pipe wall and/or volatilization from the solution.

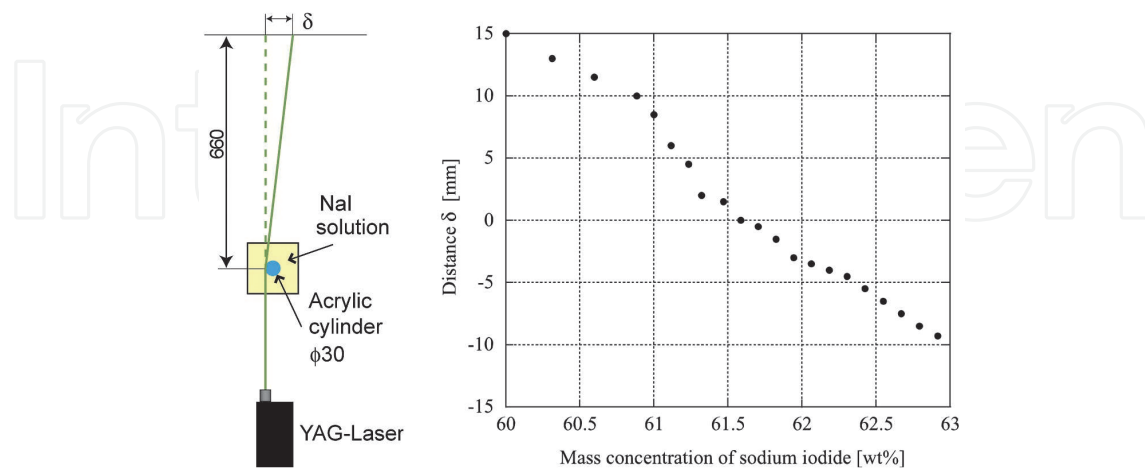


Fig. 1. Matched refractive-index experiment using NaI

2.2 PIV measurement with fluorescence particles

The PIV utilized in this experiment is a double-pulse YAG laser system manufactured by Japan Laser Corporation. The laser output is 25mJ@532nm and the maximum oscillatory frequency is 30Hz. In the PIV measurement, a time series of tracer particles' images in a sheet laser is taken with a high speed camera, and, then, a two-dimensional flow structure is quantitatively visualized from the movement of the tracer particles. The time interval of the double pulse and the tracer concentration are adjusted depending on the flow conditions. To process the obtained particle images, a cross-correlation scheme is adopted to get spatially dense velocity information. Furthermore, melamine fluorescence resin particles with 1~20 μm diameter are utilized as the tracer particles. The specific gravity of NaI solution at the above mentioned concentration is relatively close to that of this tracer, so that buoyancy influence can be ignored. When this fluorescence particle is irradiated with the YAG laser, it causes excitation in the fluorescent agent which emits light of 580nm wavelength. By taking only this newly emitted light into a CCD camera with an attached filter lens, it makes it possible to obtain a clearer particle image than the usual tracer image, because the diffused reflection light of the laser observed on the pipe wall surface and on the acrylic sphere surface can be completely removed simultaneously.

3. Experimental apparatus and details of test section

Figure 2 shows a diagram of the apparatus for the visualization experiment under isothermal conditions. The apparatus consists of the following components: a circulating pump, a flow rate measuring section, a flow-straightened section, a test section, a bag filter, and a mixing tank. All piping materials and components have been made of polyvinyl chloride or acrylic materials etc. which co-exist in a stable state with the NaI solution. The magnetic pump circulates the working fluid inside the loop, and its maximum flow rate under obstacle-unpacked conditions is approximately 200l/min. The flow rate of the working fluid is adjusted

by valves: two valves located between the magnetic pump and the flow rate measuring section and a valve of a bypass line which directly returns to the mixing tank from the magnetic pump. A turbine flowmeter or an ultrasonic Doppler velocimeter is utilized to measure the flow rate. The mixing tank has the following functions: injection of tracer particles, de-aeration of bubbles existing in the fluid, and heat exchange to control the fluid temperature. The section upstream of the test section has a flow-straightener with a honeycomb structure consisting of stainless steel pipes, which straightens and counteracts a swirling flow formed in the bend upstream. The bug filter is a polypropylene-made cartridge with strong corrosion resistance which separates the tracer particles from the NaI solution.

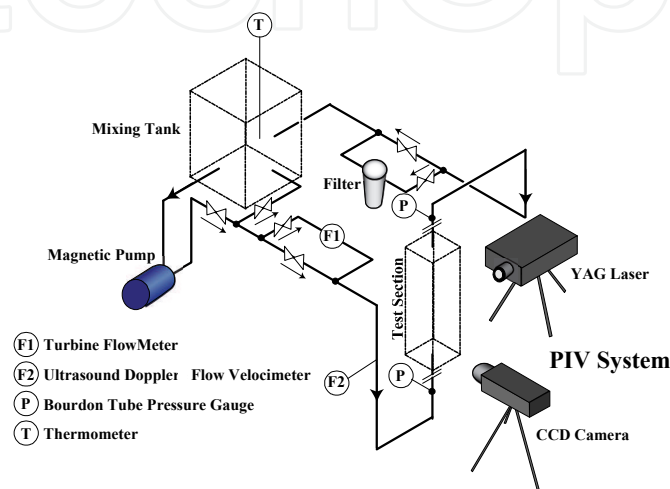


Fig. 2. Experimental apparatus for visualization

Figure 3 shows a detailed view of the visualization test section. Here, we focus here on the flow field in a Sphere-Packed Pipe (hereafter, SPP) that is utilized as a heat exchanger and/or a cooling device in various fields (e.g. Yuki et al. 2007, 2008). The test section is an acrylic vertical riser-pipe with $D=56\text{mm}$ as inner diameter and 670mm in length. The visualizing area is located at $8.2D (=460\text{mm})$ downstream from an inlet of the test section where a fully-developed flow is anticipated. In addition, there is a rectangular jacket surrounding the test section in order to reduce image distortion resulting from the geometry of the circular pipe. The NaI solution at the same temperature as the working fluid is also filled into the jacket. In order to visualize the flow field in the lateral cross section of the circular pipe, an acrylic observation window is attached to the upper part of the test section. Figure 2 also shows the packing structure of the acrylic spheres. The sphere size prepared for this research is $D/2.0$ (27.6mm) in diameter, and 68 spheres can be packed in the test section with a porosity of 0.548. An acrylic baffle plate set between the flanges, which exist at the inlet and outlet of the test section, fixes the acrylic spheres.

The temperature of the NaI solution is 30 degrees Celsius, and the visualization of the flow field is conducted at three Reynolds numbers ($Re_d=Ud/\nu$) of 800, 2000 and 4900, based on the sphere diameter, d , and mean inlet-velocity U . The mean inlet-velocity, which is equivalent to superficial velocity in the SPP, is 0.0376, 0.0940 and 0.230 m/s, respectively. Fand et al. (1990, 1993a, 1993b) have classified the SPP pipe flow with $D/d>1.4$ into: turbulent regime ($Re_d>120$), Forchheimer regime ($5<Re_d<80$), and Darcy regime ($Re_d<2.3$) from the data of friction factor. In that sense, the flow conditions in this research could be in the turbulent regime. This fact was also confirmed by the authors' experiments (Yuki et al., 2005).

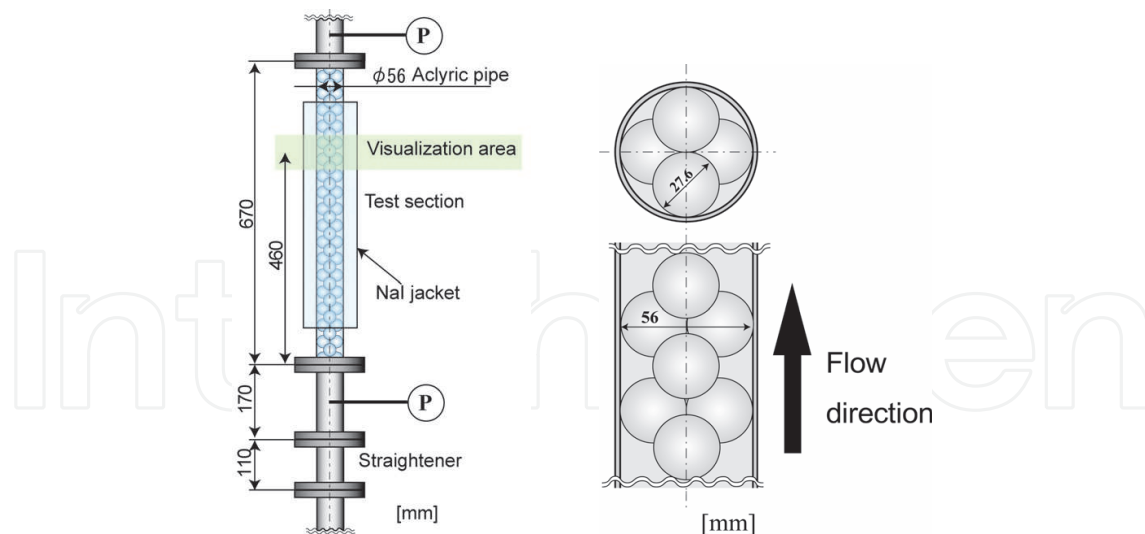


Fig. 3. Test section and packing structure

4. Flow-structures in sphere-packed pipe

4.1 Flow structures in a central longitudinal-section

First, a central longitudinal section S_1 shown in Figure 4 is visualized. Figure 5 shows a time-series of the flow fields at the lowest Re number of $Re_d=800$. The matched refractive-index method makes it possible for the flow field in the central area of the pipe, which is usually impossible to see, to be successfully and vividly visualized. The whole flow field fluctuates intensely and is extremely unsteady. In order to discuss the flow field more qualitatively, the time-averaged flow field is shown in Figure 6(a). This clearly provides that a high-velocity flow spouting from the upstream of a central area A (spouting flow, hereafter) is pushed back toward the center area again from around the middle of the center area and the wall. Furthermore, judging from the instantaneous flow fields together, a flow toward the pipe wall, which is considered as a part of a wake, forms a strong impinging flow to the pipe wall. After this impingement, a backward-flow in the upstream direction forms a circular vortex in the area B between the sphere and the wall. It can be also confirmed that there exists a small circular vortex behind the impinging flow. An interesting feature is the formation of a low-velocity area in the middle of the spouting flow and the impinging flow, which seems to capture a coexisting area of different kinds of several flows in the SPP. In addition, there is stagnation in the area C closely located to the contact point between the sphere and the wall. If the SPP is utilized

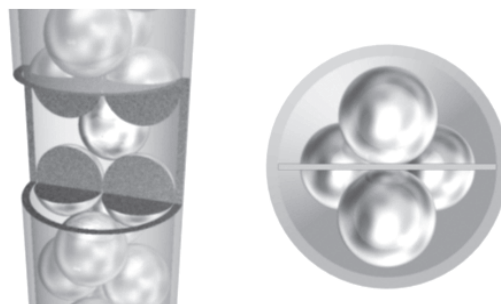


Fig. 4. Visualizing section: S_1

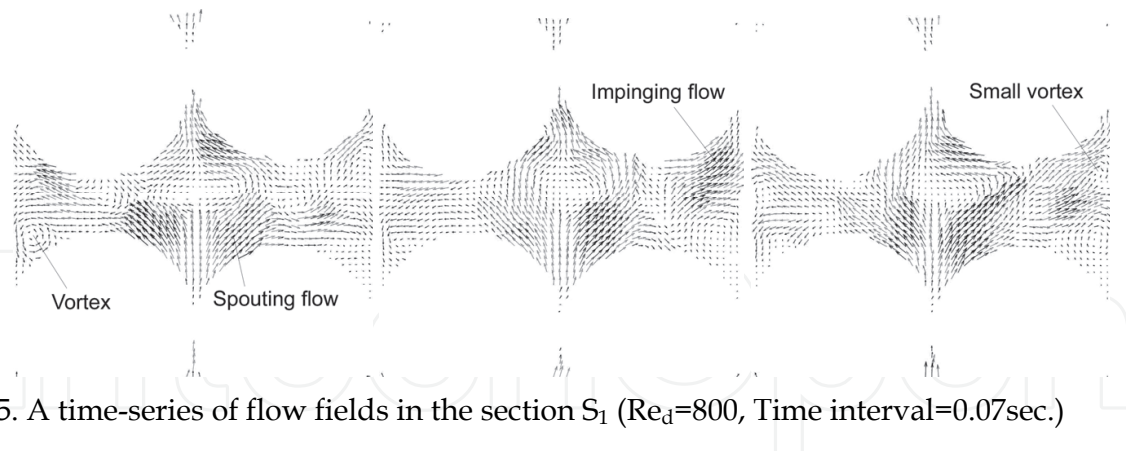


Fig. 5. A time-series of flow fields in the section S_1 ($Re_d=800$, Time interval=0.07sec.)

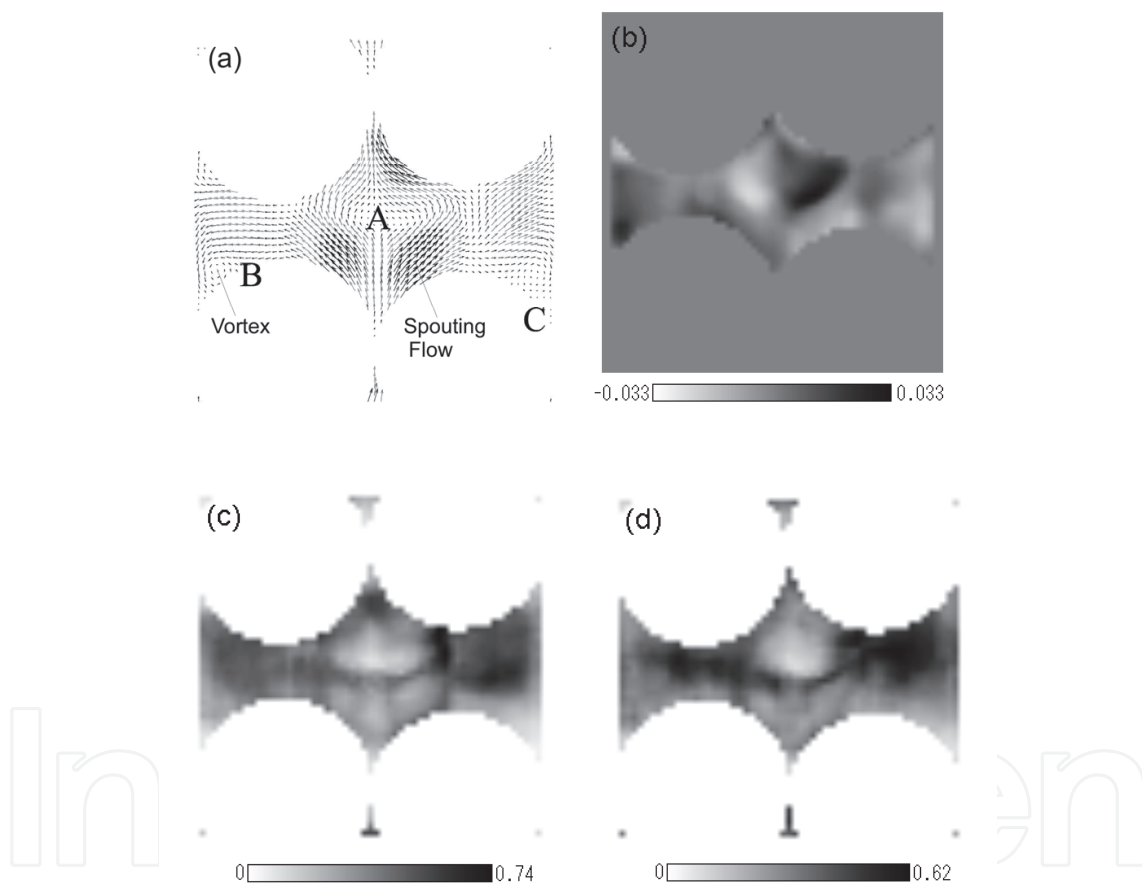


Fig. 6. Time-averaged flow field (a), vorticity (b), and intensity of velocity fluctuation (c): U_p & (d): V_p

as a heat transfer promoter, it is impossible to remove enough heat in this area under the heating conditions, so that the wall-temperature could rise sharply here, especially for higher Pr number fluid. However, the area downstream of this stagnation seems to have a high heat transfer performance due to the effect of the impinging flow. Figure 6(b) shows vorticity distribution for the time-averaged flow field. The regions around A and near the wall with high vorticity hold a high heat transport performance. Hence, the spouting flow

around the central area and its returning effect efficiently transport enthalpy that was transported from the heating wall by the circular vortex toward the center of the pipe, which could work more effectively if there existed active heat conduction from the wall to the sphere. Figures 6(c) and (d) respectively represent intensities of velocity fluctuation in the radial and streamwise directions, U_p and V_p , which are calculated by RMS and normalized by each inlet velocity U . A strong velocity-fluctuation area is formed upstream of the sphere existing downstream. Their maximum values over 0.6 indicate that the intensity of this variation is quite high. These fluctuations could significantly contribute to the heat transport from the wall, because both the areas with high velocity fluctuation spread toward the pipe wall.

Figures 7 present two kinds of profiles at the horizontal center line of the visualizing area: the one is the averaged velocity profile about u and v in the radial and streamwise directions and the other is the RMS profiles of velocity fluctuation U_p and V_p . The radial velocity near the wall indicates the strength of the impinging flow and is higher than the inlet velocity. The velocity profiles at $Re_d=4900$ differ from the other cases at $Re_d=800$ and 2000, and indicates a lower value, especially near the wall. This is conceivably because the impinging flow area moves more downstream at $Re_d=4900$. As to the streamwise velocity profile, the spouting flow around the center area is accelerated as the Re_d number increases. Both figures show that the velocity peak position near $x/R=\pm 0.25$ shifts toward the center of the pipe with increasing Re_d number, which suggests the prevention of the spread of the spouting flow and also suggests the development of something strong flow pushing the spouting flow back. Additionally, there are two areas with high velocity fluctuation near $x/R=\pm 0.5$ for each Re_d number, which indicates that the above-mentioned two characteristic flow-structures themselves have strong variation and are closely linking with each other

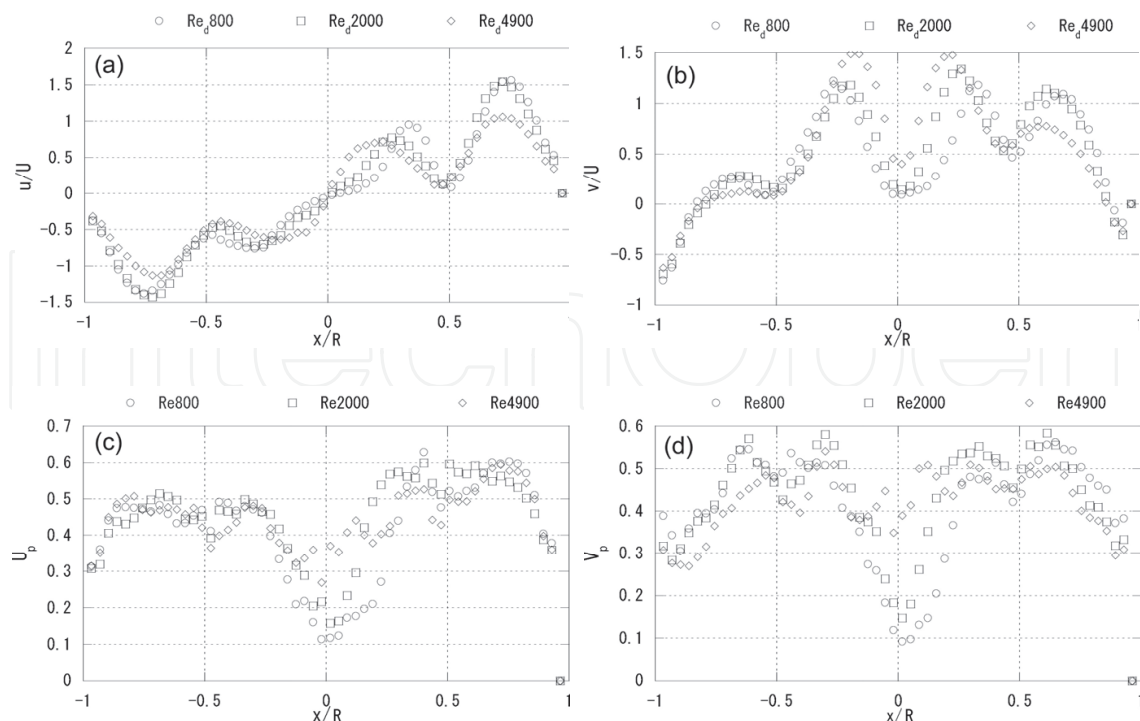


Fig. 7. Mean velocity and velocity-fluctuation intensity profiles in the radial and streamwise directions

because of there not being much difference in the variation in both the flow structures. In all data, there exists low flow velocity and a low velocity fluctuation area at the location of $x/R=\pm 0.5$. This location corresponds to the coexistence area for the two flow structures that seems to exist around the right and left sides of the sphere existing in front and back of the A area. The flow structure in this coexistence area will be clarified later by comparison with the flow structures on the other cross sections.

4.2 Flow structure of bypass flow due to wall effect

Since the present SPP has four wide gap-channels in the streamwise direction due to the existence of the pipe wall, the flow characteristics of a high-velocity channeling flow, that is to say a bypass flow formed in this area, strongly affect not only the flow structures of the spouting flow and the vortices behind the sphere but also heat transfer characteristics. To capture this flow, a longitudinal section S_2 shown in Figure 8 is visualized. Figures 9(a) through (d) are the distributions of time-averaged flow field, vorticity, and the RMS of velocity fluctuations, respectively, in the right half area of the S_2 at the Re_d of 800. The bypass flow flowing in parallel with the pipe wall is observed in the gap area between the sphere and the pipe wall. The wake area behind the sphere has high vorticity, because the flow direction shifts to the back from the front of the paper depending on the packing structure, as well as the influence of the wake. In addition, the RMS of velocity fluctuation, U_p and V_p , are more overwhelmingly intense than those in the case of the above mentioned longitudinal section S_1 , which indicates strong unsteadiness of the flow field in this section, especially beside and behind the sphere. A time-series of the flow fields allow us to confirm that a circular vortex or a flow with low velocity is intermittently formed in this area (note: this is caused by strong variation at the bend of the bypass flow described later on). To quantitatively evaluate the influence of the Re_d number on the flow structure of the bypass flow, Figures 10(a) through (d) show the flow velocity profiles and the RMS of velocity fluctuation in the radial and streamwise directions at the horizontal center line in the middle of S_2 . Minus value of the radial flow velocity means that the sphere shape contributes to a certain amount of momentum transfer toward the center of the pipe. Additionally, Figure 10 (b) shows that the bypass flow has quite a high velocity, whose maximum value is around 6 times that of the mean velocity. The Re_d number doesn't seem to affect the value much. Judging from this, it is evident that the bypass flow could be the something strong flow for the spouting flow being pushed back and for producing some vortices including the impinging flow. Though the RMS of velocity fluctuation in both the radial and streamwise directions goes up as the Re_d number increases, the data at $Re_d=800$ shows a peculiar profile. It is considered that the flow field at $Re_d=800$ still has the characteristics in lower Re_d number regime where there exists a different kind of vortex shedding behind the sphere.

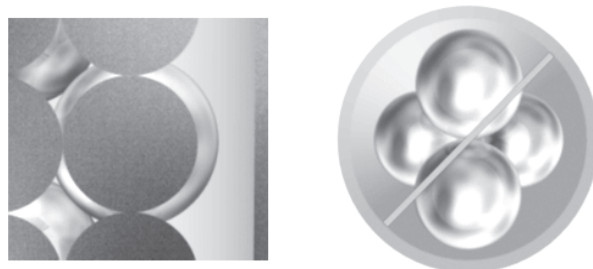


Fig. 8. Visualizing section: S_2

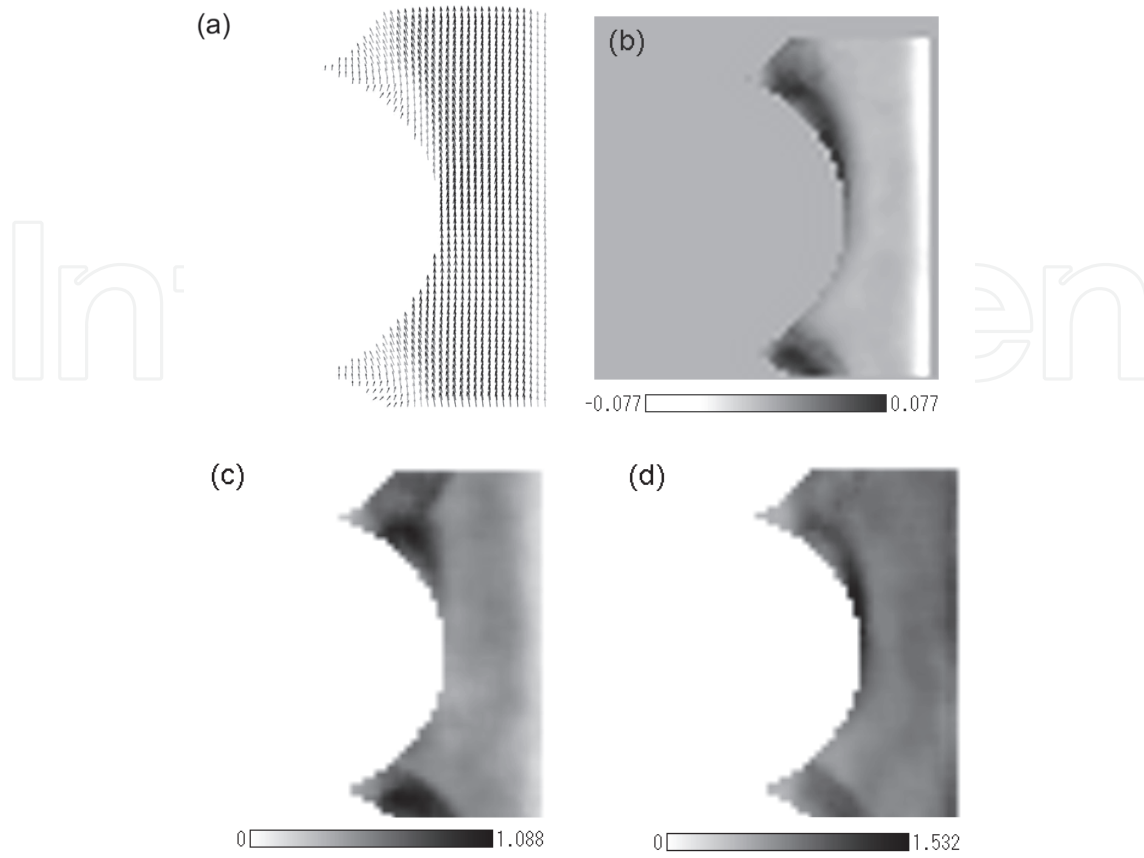


Fig. 9. Time-averaged flow field, vorticity, and RMS of velocity fluctuation of bypass flow

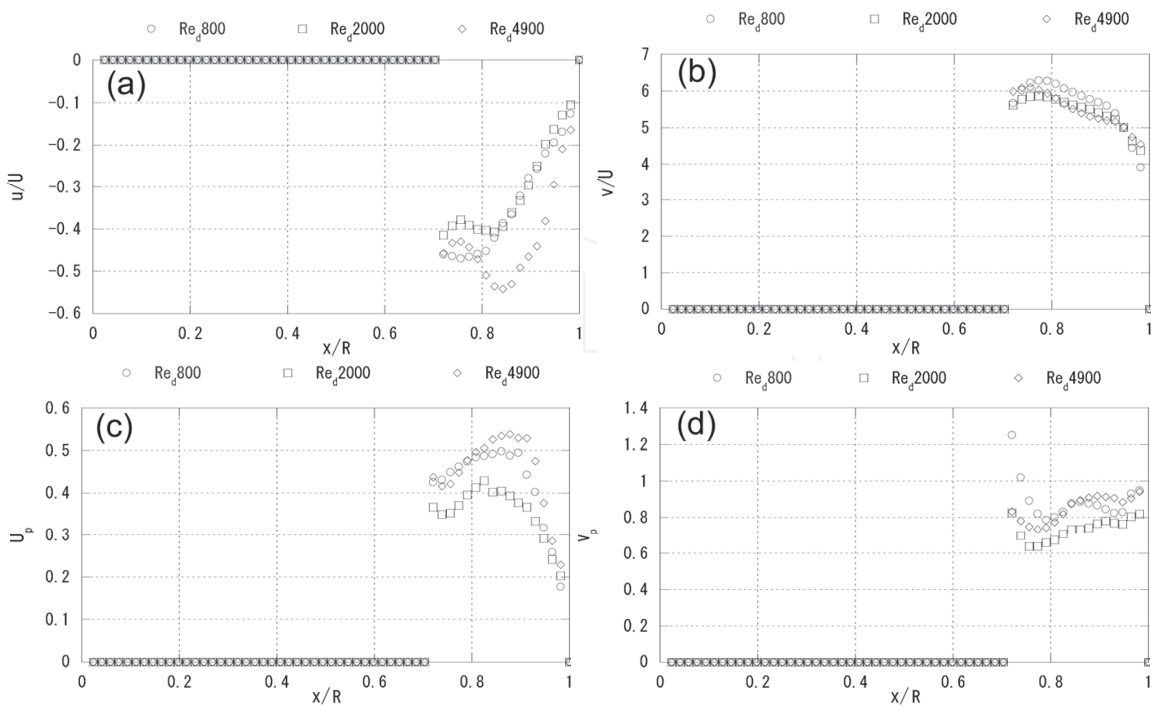


Fig. 10. Mean velocity and RMS profiles in the radial and streamwise directions

To evaluate the three-dimensional structure of the bypass flow, the flow field in the longitudinal section S_3 perpendicularly to S_2 is focused on (see Figure 11). Figures 12(a) through (d) show the same distributions as those of Fig.11. The bypass flow is flowing with a meandering motion through the spheres in a circumferential direction. Furthermore, a circular vortex is formed between the upstream and downstream spheres. As this circular vortex is formed near the downstream sphere, the flow that is branched by the meandering bypass flow colliding with the downstream sphere significantly plays a role in forming the vortex. In addition, the existence of a high-vorticity area A being released from the sphere represents the boundary of the bypass-flow route. Regarding the velocity fluctuation U_p in the horizontal direction of S_3 , the area with high velocity fluctuation is formed on the bypass-flow route, which means that the bypass flow itself unsteadily changes in the circumferential direction. Furthermore, an area B with high velocity fluctuation is formed forward of the downstream sphere. As already described, a part of the bypass flow collides with the downstream sphere due to its meandering motion. In such areas, the flow becomes unstable and increases the intensity of velocity fluctuation by the influence of the sphere geometry. Regarding the intensity of velocity fluctuation V_p in the vertical direction of S_3 , an area C with high velocity fluctuation exists beside the bypass-flow route between the upstream and downstream spheres. The flow loses stability in this large gap area by being released from the influence of the upstream sphere-surface, which could also lead to the formation of the impinging flow mentioned before though this flow can't be confirmed in this section S_3 . Figure 13 is a time-series of the flow fields at $Re_d=4900$. Looked at through the time-averaged flow field characteristics, the flow structures don't show such significant change as is the case at $Re_d=800$. However, the time-series of the flow fields show that two apparent circular vortices are formed between the downstream and upstream spheres. In other words, the wake structure in the large gap area between the spheres is characterized by the co-existence of the circular vortex formed by the colliding effect of the bypass flow with the downstream sphere and by the separation vortex shedding from the upstream sphere. In particular, the small vortex shown in Fig. 5 corresponds to a part of this downstream vortex. The existence of these two vortices has been also confirmed at $Re_d=800$. In the SPP flow, it is quite interesting that several vortices exist between the upstream and downstream spheres. In addition, the bypass-flow seems to meander in larger area with increasing Re_d number as shown in Figures 14(c) and (d), which show the RMS of the velocity fluctuation in the horizontal and vertical directions at the horizontal center line of S_3 . In Fig. 14(a), the horizontal velocity indicates a minus value because of the separation vortex near the wall. Observing from the streamwise velocity profiles in Fig. 14(b), the maximum flow velocity of the bypass flow is almost 5 through 6 times higher than the mean velocity, regardless of the Re_d number. This fact accords with the result shown in Figure 10(b). Moreover, the central axis of the bypass flow also seems not to be influenced by the Re_d number, because the peak location of the streamwise velocity doesn't shift for the change in the Re_d number.



Fig. 11. Visualizing section: S_3

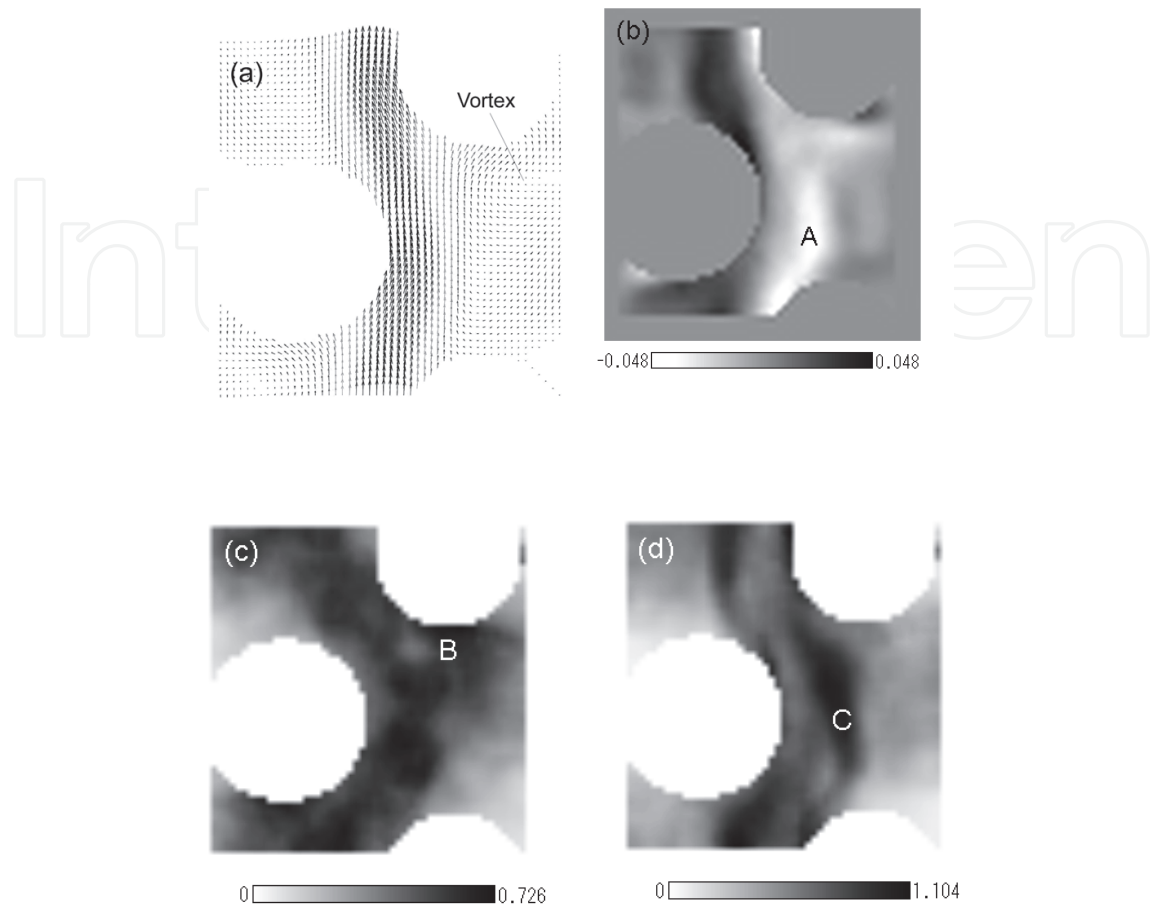


Fig. 12. Time-averaged flow field, vorticity, and RMS of velocity fluctuation of bypass flow

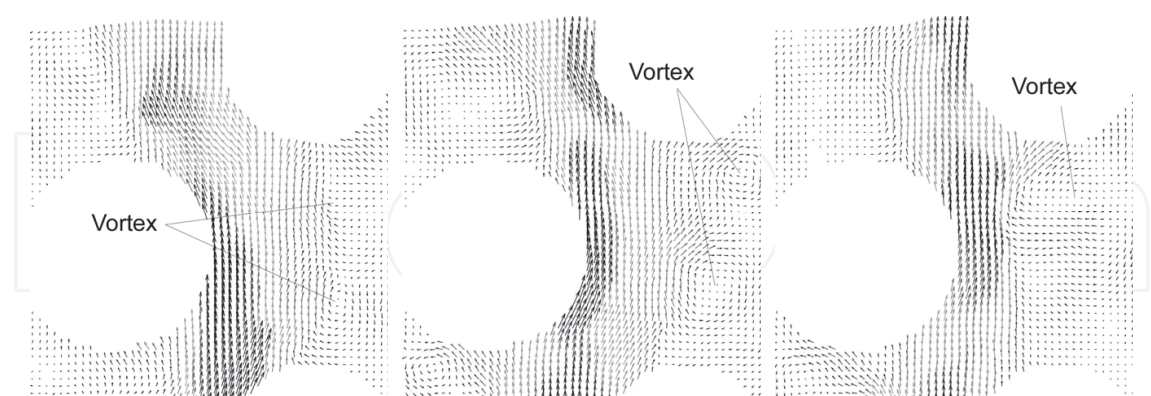


Fig. 13. Time sequence of flow fields of bypass flow ($Re_d=4900$, Time interval=0.07sec.)

4.3 Flow structure behind the sphere

To identify further the wake structures formed between the spheres, the longitudinal section S_4 shown in Figure 15 is visualized. Figure 15 also show instantaneous flow fields at $Re_d=4900$, and Figures 16(a) through (c) show the distributions of vorticity and intensities of velocity fluctuation in the horizontal and vertical directions of S_4 , respectively. The high-

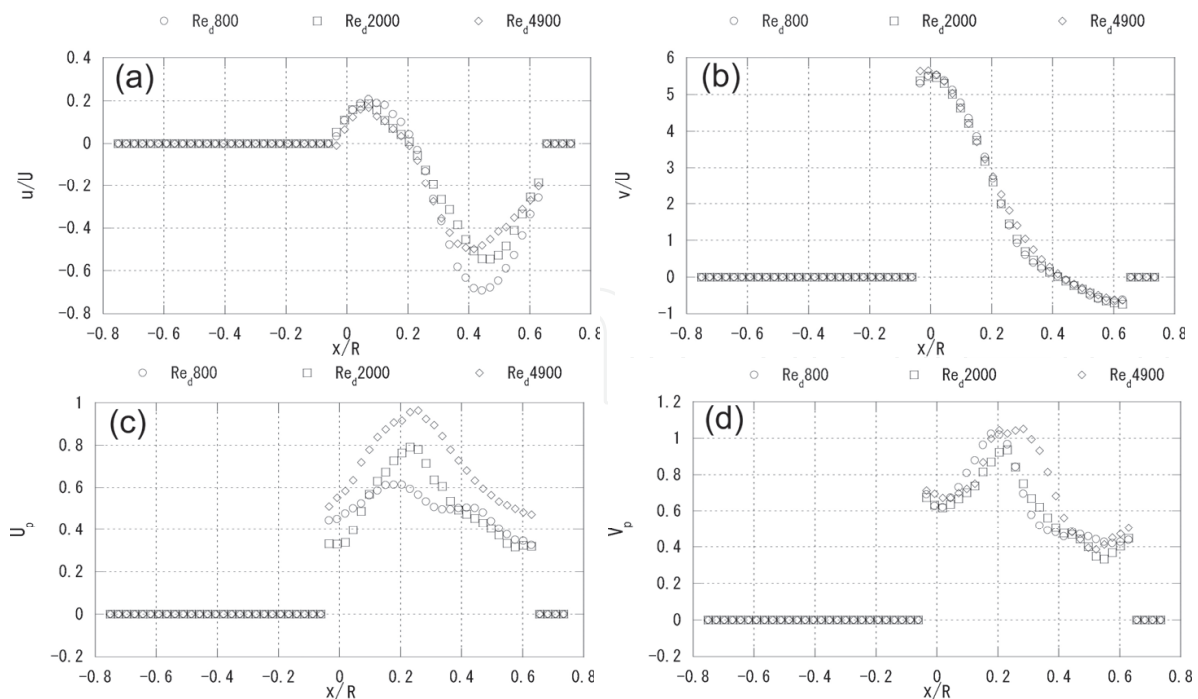


Fig. 14. Mean velocity and velocity-fluctuation intensity profiles in horizontal and vertical directions of S_3

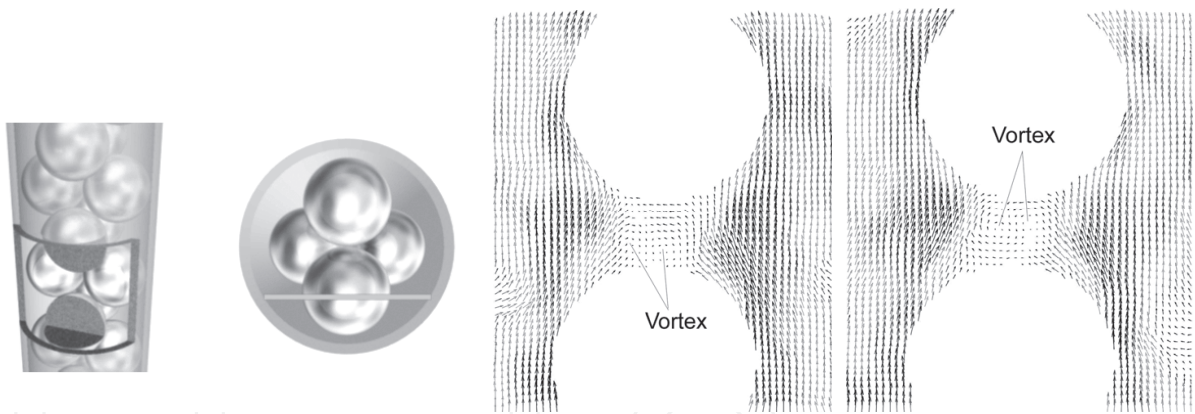


Fig. 15. Visualizing section: S_4 and instantaneous flow fields behind sphere ($Re_d=4900$, Time interval=0.07sec.)

velocity flow existing in the gap between the sphere and the pipe wall is the bypass flow itself. Observation through the instantaneous flow fields confirms the generation and disappearance of a circular vortex such as Karman-like twin vortices behind the sphere that is strongly affected by the inflowing of a part of the bypass flow. According to this inflowing, an area with high vorticity exists behind the sphere as shown in Fig. 16(b). The shape and behavior of these vortices are another aspect of the separation vortex mentioned above. However, as it is difficult to visualize both the two kinds of vortices simultaneously, the downstream circular vortex, which should be also twin vortices, seems to be somewhat flat in the circumferential direction and be formed near the pipe wall as shown in Fig. 5. In addition, the gap area between the spheres has high velocity fluctuation, this also indicates strong time variation of these two pairs of twin vortices. These vortices don't affect the

bypass flow structure and its behavior significantly, because the area with high velocity fluctuation by the wake does not spread out to the bypass flow area. To sum up the matter, there are two factors that form the structure of the wake between the spheres and their unsteady behavior (see Fig. 16(d) that is illustrations of flow structures in S_3 and S_4): 1, Twin separation vortices shedding from the sphere in the process that a part of each high-velocity bypass flow passing beside the sphere flows into the large gap area located behind the sphere (this process also generates the strong impinging flow as mentioned later on); 2, Twin circular vortices generated by the colliding and branching effects of two bypass flows in front of the sphere in downstream.

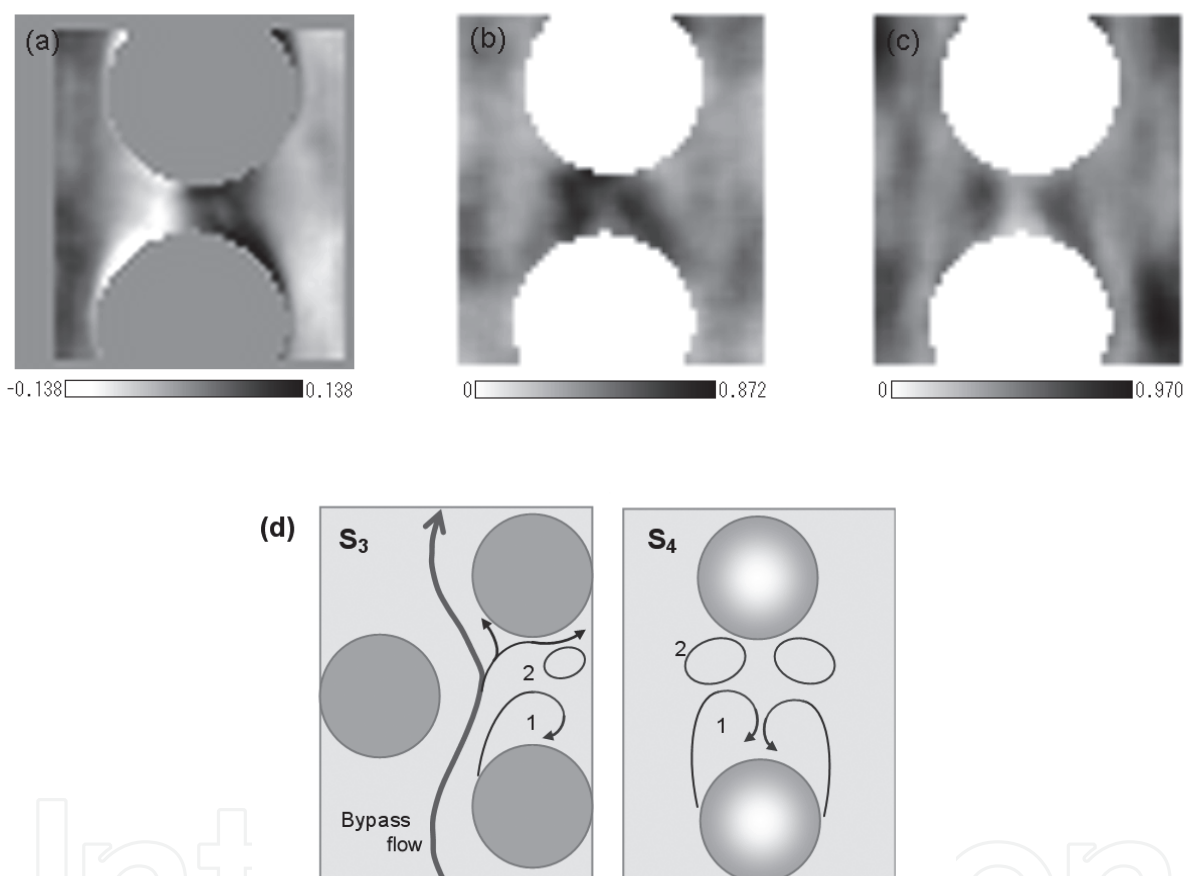


Fig. 16. Vorticity & velocity fluctuations ($Re_d=4900$), and illustration of flow structure in S_3 & S_4

4.4 Flow structure in a cross section of circular pipe

Finally, the flow fields in a lateral cross section of the pipe, i.e. a secondary flow, are visualized in order to investigate the three-dimensional structure of the flow field in the SPP. The matched refractive-index PIV method only enables to observe the flow field in this cross section. Figure 17 shows a time-series of the secondary flows at the Re_d numbers of 800 and 4900 in the lateral cross section, S_5 , perpendicular to the longitudinal section S_1 (see Fig. 17 on the lower right). These figures clearly show that apparent twin vortices with strong variation exist in the lateral cross section. The four circled areas in the time-

averaged flow field at $Re_d=800$ in Fig. 17 on the upper right are the ones for the bypass flow passing through. As already mentioned, the bypass flow meanders along the sphere geometry and a part of it flows into the large gap area between the upstream and downstream spheres, so that it is obvious that the bypass flow becomes a significant driving flow for the twin vortices. Additionally, the strong flow toward the wall, which is in the middle of the twin-vortices, corresponds to the impinging flow confirmed in cross section S_1 . In other words, the two bypass flows heading toward the large gap area, after passing through the upstream sphere, generate the twin-vortices that correspond to the upstream separation vortices. Since there is one more pair of twin vortices downstream due to the colliding effect of the two bypass flows with the downstream sphere, these two different twin vortices form three-dimensional structures in the gap area. On the other hand, the velocity vectors of the spouting flow from the pipe center observed in the cross section S_1 have not been confirmed. It is predicted that the bypass flow toward the gap area pushes back the spouting flow toward the pipe center again in this section S_5 . As a result, the low-velocity area in the upstream of the impinging flow is formed in the circled areas. Although the spouting flow tries to spread out also in a circumferential direction, it heads toward the opposite direction against the rotating direction of the twin-vortices.

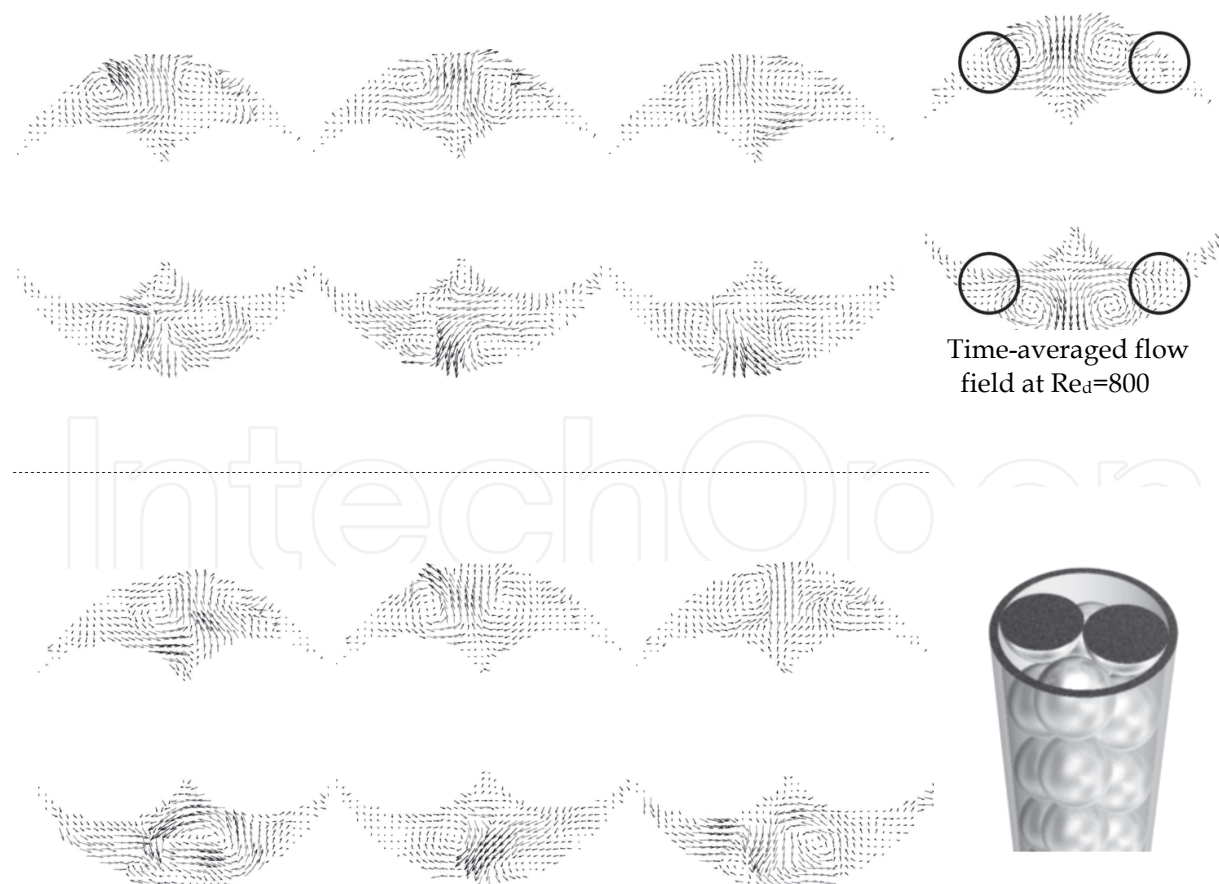


Fig. 17. Time-series of secondary flows (Upper: $Re_d=800$, Lower: $Re_d=4900$, Time interval=0.07sec.)

The multiple vortices with the above mentioned complex structure could have strong effects on the fluid mixing and heat transport from the heating wall, which suggests that control of the bypass flow plays an important role in heat transfer augmentation of the SPP.

5. Other application of the matched refractive-index PIV method

The matched refractive-index PIV method easily enables to visualize various kinds of complex flow structures. As the second application of this method, we focus on a flow separation formed in a curved pipe with a low curvature ratio. Figure 18 shows the longitudinal flow fields in the curved pipe and its downstream circular pipe region (Yuki et al., 2009). The Re number is approximately 50,000 (inlet mean velocity is 0.78 m/s). This flow condition corresponds to a subcritical regime defined by Idelchik (1986). The test section was made from an acrylic rectangular block where the curved flow-channel is manufactured by 3D-NC cutting. The pipe diameter is 56mm. The entrance section to the curved pipe is a circular straight pipe with a length of 50 times as long as the pipe inner diameter so that the fluid flow going into the test section becomes an almost fully developed turbulent flow. The curvature ratio of the curved pipe is 1.0 ($=R/D$: where R is the curvature radius). Here, we introduced an infrared ray Diode laser, with an output of 10mJ and a wavelength of 808nm. This indicates that the refractive-index of the NaI solution needs to be re-adjusted with the method shown in Figure 1. Nylon particles with the average diameter of 20 μ m and a specific gravity of 1.03 are used as the tracer particle. Figures 18(a), (b), (c), and (d) show the instantaneous flow fields, time-averaged flow field, velocity contour lines map, and the RMS distribution of velocity fluctuation in the longitudinal section of the curved pipe and its downstream, respectively. As the accuracy of PIV measurement near the outlet area of the curved pipe drastically degrades due to existence of an O-ring, a rectangular white box is put on it. The high velocity flow produced by a centrifugal force oscillates in an unsteady manner, and this oscillation is conceivably self-induced one due to flow instability by loosing a balance between a centrifugal force and a pressure gradient especially near the inlet area of the curved pipe. The highest velocity is confirmed near the inner wall of the inlet, due to the favorable pressure gradient toward the streamwise direction. The maximum velocity reaches 1.12m/s which is 1.44 times as the inlet mean velocity. Moreover, a low-velocity area on the inner wall side that is considered to be a part of the flow separation develops from around 40 degree of angle from the elbow inlet (see the time-averaged flow field). The instantaneous flow fields also show a counter flow structure that can be regarded as a part of the separation vortex. The low-velocity area develops toward the downstream of the curved pipe, and along with that, it is confirmed that the flow field in the central area is accelerated again in the outlet region. The separation point exists at a more upstream position, compared with the previous research results (Shiraishi et al., 2006). This is because the turbulent flow with a fully developed boundary layer flows into the curved pipe, unlike the previous research whose inlet flow has an almost uniform velocity profile. Focusing on the flow structure of the low velocity region, Figure 18 clearly show that the low-velocity area with a complicated unsteady flow exists on the inner wall side of the curved pipe and develops toward the downstream circular pipe region. Furthermore, comparatively small transverse vortices are repeatedly generated and disappeared in the upstream shear layer of the low-velocity area (hereafter, a separation region), which increases the RMS of velocity fluctuation as shown in Figure 18(d). In

In addition, much larger flow structures exist in the downstream of the low velocity region. In particular, this larger flow structure significantly and unsteadily changes near the wall of the circular pipe (the RMS value is around 0.4), which is likely to reflect a part of the shedding behavior of separation vortices that have been pointed out by the previous research. In fact, the Strouhal number, $fD/U_m \sim 0.59$ ($f=8.2\text{Hz}$), is almost the same as that estimated by Iwamoto et al. (2008). The time-average flow field shows that the velocity becomes higher again in this strong fluctuating region (hereafter, a velocity recovery region). The starting point of the velocity recovery is approximately $0.33D$. Namely, since the high-velocity fluids transferred from the central area of the curved pipe by the secondary flow through the side walls collide each other around this area, the unsteadiness of the flow field becomes much more significant.

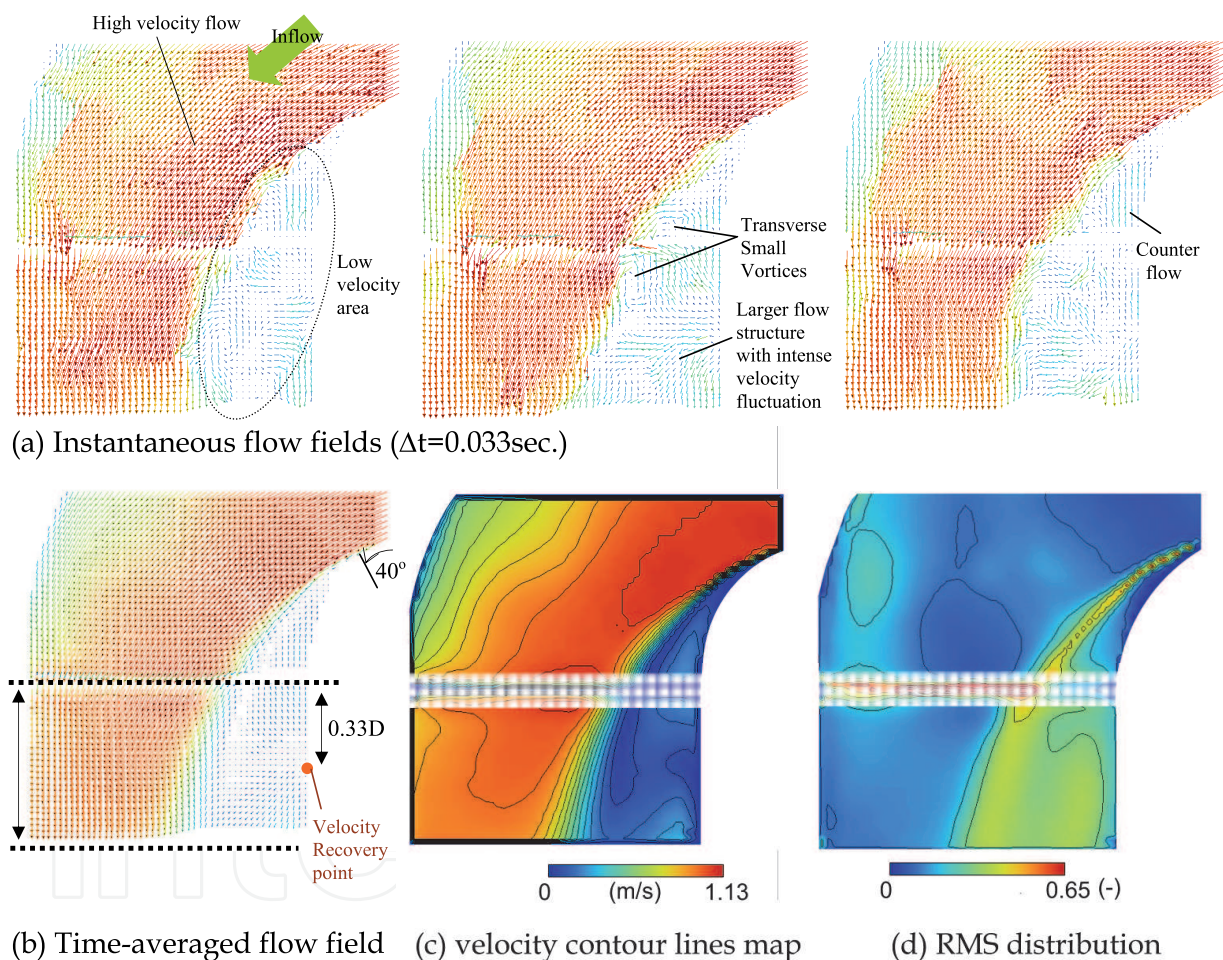
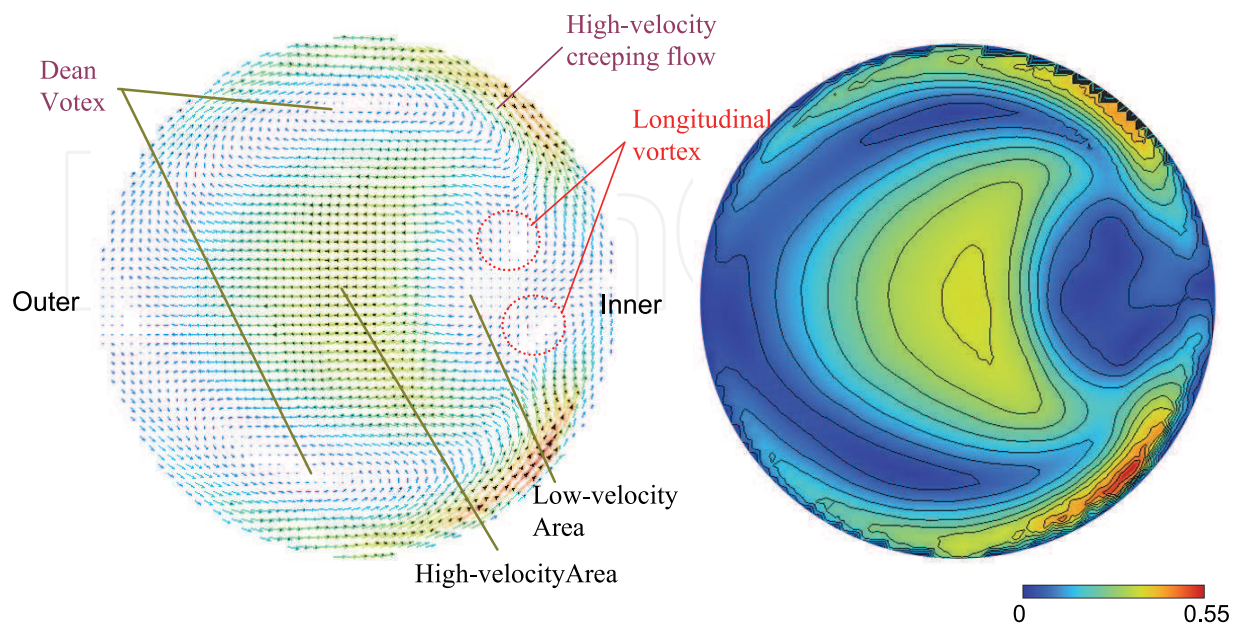


Fig. 18. Flow structure in a curved pipe and its downstream close-up of low velocity region

To clarify the three-dimensional structure of the separation region, the secondary flow is visualized at the $0.18D$ downstream of the outlet of the curved pipe (see Fig. 19). A low-velocity area exists between the high-velocity area formed in the pipe center and the inner wall. Furthermore, two pairs of characteristic twin vortices can be confirmed. The larger twin vortices are Dean vortices generated by the centrifugal force, whereas the smaller twin vortices formed near the inner wall represent the lateral structure of the separation region. In other words, the flow structure at this location has not only the transverse



(a) Time-averaged flow field

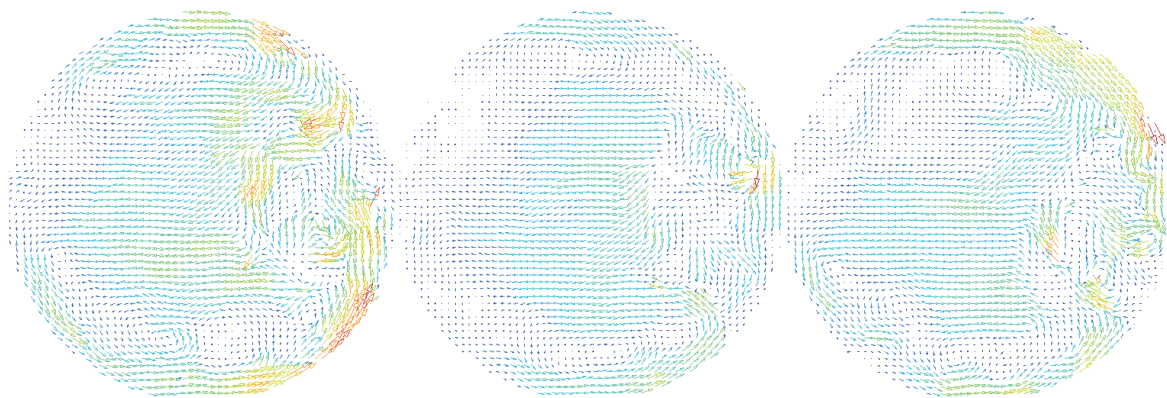
(b) Instantaneous flow fields ($\Delta t=0.33$ seconds)

Fig. 19. Secondary flow structure shortly after 1st elbow

vortices but also two longitudinal vortices. Moreover, a high-velocity flow that exceeds 70% of the inlet mean flow velocity exists around the side walls (hereafter, a high-velocity creeping flow). This high-velocity creeping flow alternately flows into the separation region, so that the flow field in the velocity recovery region could become more unsteadily, accompanied with complicated large vortices. Although further investigation should be conducted to clarify in what part of the elbow this high-velocity creeping flow is formed, there could be the possibility that this flow is formed to complement the fluid defect along with the shedding of the separation vortices. Whichever the case may be, there is no doubt that this high-velocity creeping flow has a significant impact on the flow

structure of the velocity recovery region and the dynamic behavior of the vortex shedding as well.

6. Conclusions

In this chapter, I introduced the matched refractive-index PIV measurement to visualize complex flow structures. The visualization was conducted by matching refractive-index of working fluid to that of an obstacle and/or the piping material. Here, flow structures in a sphere-packed pipe and a curved pipe were focused on as the examples, the interesting flow structure became obvious. Although the NaI solution was utilized here, some other solutions are also available or special materials with the same refractive index of the working fluid could be useful. For instance, FEP material has the same refractive index as that of water. The matched refractive-index visualization technique enables to understand not only a 3-dimensional time-series of complex flow structures with complex geometry by utilizing a stereo type of dynamic PIV technique but also a two-phase flow in the near future.

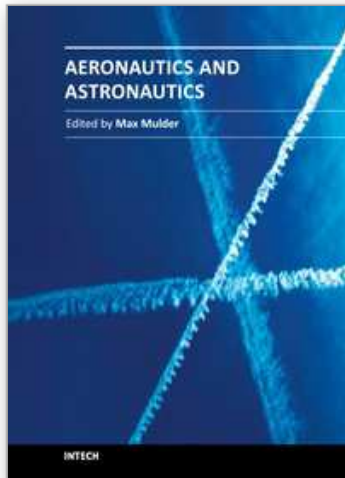
7. References

- K. Yuki, et al. (2007). Heat transfer performance for high Prandtl and high temperature molten salt flow in sphere-packed pipes, *Fusion Science & Technology*, vol. 47, no. 4, pp. 1089-1093.
- Kazuhisa Yuki, et al. (2008). Heat transfer enhancement in sphere-packed pipes under high Reynolds number conditions, *Fusion Engineering and Design*, vol. 83, Issues 7-9, pp. 1102-1107.
- R. M. Fand & R. Thinakaran (1990). The influence of the wall on flow through pipes packed with spheres, *Journal of Fluids engineering*, vol. 112, pp. 84-88.
- R. M. Fand, M. Sundaram, M. Varahasamy (1993). Incompressible fluid flow through pipes packed with spheres at low dimension ratios, *Journal of Fluids engineering*, vol. 115, pp. 169-172.
- R. M. Fand, M. Varahasamy, L. S. Greer (1993). Empirical correlation equations for heat transfer by forced convection from cylinders embedded in porous media that account for the wall effect and dispersion, *International journal of heat mass transfer*, vol. 36, no. 18, pp. 4407-4418.
- K. Yuki, et al. (2005). Evaluation of flow structure in packed-bed tube by visualization experiment, *Fusion science and technology*, vol. 47, no. 4, pp. 1089-1093.
- Kazuhisa Yuki, et al. (2009), Unsteady Hydraulic Characteristics in Large-Diameter Piping with Elbow for JSFR, (3) Flow Structure in a 3-Dimensionally Connected Dual Elbow Simulating Cold-Leg Piping in JSFR, *Proceedings of the 13th International Topical Meeting on Nuclear Reactor Thermal Hydraulics*, N13P1167.
- Idelchik, I. E. (1986). *Handbook of Hydraulic Resistance, 2nd edition.*, Hemisphere, New York, p.271.
- T. Shiraishi et al. (2006). Resistance and Fluctuating Pressures of a Large Elbow in High Reynolds Numbers, *Journal of Fluids Engineering*, vol. 128, pp. 1063-1073.

- Y. Iwamoto et al. (2008). Study on Flow-Induced-Vibration Evaluation of Large-Diameter Pipings in a Sodium-Cooled Fast Reactor (4) Experiments on the 1/10-Scale Hot Leg Test Facility in Reynolds Number of 50000 and 320000, *Proceedings of Japan-Korea Symposium on Nuclear Thermal Hydraulics and Safety (NTHAS6)*, N6P1010.

IntechOpen

IntechOpen



Aeronautics and Astronautics

Edited by Prof. Max Mulder

ISBN 978-953-307-473-3

Hard cover, 610 pages

Publisher InTech

Published online 12, September, 2011

Published in print edition September, 2011

In its first centennial, aerospace has matured from a pioneering activity to an indispensable enabler of our daily life activities. In the next twenty to thirty years, aerospace will face a tremendous challenge - the development of flying objects that do not depend on fossil fuels. The twenty-three chapters in this book capture some of the new technologies and methods that are currently being developed to enable sustainable air transport and space flight. It clearly illustrates the multi-disciplinary character of aerospace engineering, and the fact that the challenges of air transportation and space missions continue to call for the most innovative solutions and daring concepts.

How to reference

In order to correctly reference this scholarly work, feel free to copy and paste the following:

Kazuhiya Yuki (2011). Visualization of Complex Flow Structures by Matched Refractive-Index PIV Method, Aeronautics and Astronautics, Prof. Max Mulder (Ed.), ISBN: 978-953-307-473-3, InTech, Available from: <http://www.intechopen.com/books/aeronautics-and-astronautics/visualization-of-complex-flow-structures-by-matched-refractive-index-piv-method>

INTECH
open science | open minds

InTech Europe

University Campus STeP Ri
Slavka Krautzeka 83/A
51000 Rijeka, Croatia
Phone: +385 (51) 770 447
Fax: +385 (51) 686 166
www.intechopen.com

InTech China

Unit 405, Office Block, Hotel Equatorial Shanghai
No.65, Yan An Road (West), Shanghai, 200040, China
中国上海市延安西路65号上海国际贵都大饭店办公楼405单元
Phone: +86-21-62489820
Fax: +86-21-62489821

© 2011 The Author(s). Licensee IntechOpen. This chapter is distributed under the terms of the [Creative Commons Attribution-NonCommercial-ShareAlike-3.0 License](#), which permits use, distribution and reproduction for non-commercial purposes, provided the original is properly cited and derivative works building on this content are distributed under the same license.

IntechOpen

IntechOpen